Fortschr. Phys. **54**, No. 8 – 10, 648 – 665 (2006) / **DOI** 10.1002/prop.200610324

Optimization of segmented linear Paul traps and transport of stored particles

Stephan Schulz, Ulrich Poschinger, Kilian Singer*, and **Ferdinand Schmidt-Kaler**

Abteilung Quanten-Informationsverarbeitung, Universität Ulm, Albert-Einstein-Allee 11, 89069 Ulm, Germany

Published online 4 August 2006

Key words Quantum computation, control theory, segmented ion trap
PACS 02.30.Yy, 32.80.Pj, 03.67.Lx

Single ions held in linear Paul traps are promising candidates for a future quantum computer. Here, we discuss a two-layer microstructured segmented linear ion trap. The radial and axial potentials are obtained from numeric field simulations and the geometry of the trap is optimized. As the trap electrodes are segmented in the axial direction, the trap allows the transport of ions between different spatial regions. Starting with realistic numerically obtained axial potentials, we optimize the transport of an ion such that the motional degrees of freedom are not excited, even though the transport speed far exceeds the adiabatic regime. In our optimization we achieve a transport within roughly two oscillation periods in the axial trap potential compared to typical adiabatic transports that take of the order 10^2 oscillations. Furthermore heating due to quantum mechanical effects is estimated and suppression strategies are proposed.

1 Introduction

With a series of spectacular experiments the ion trap based quantum computing has proven its prominent position for a future quantum computer among the list of candidates [1]. Starting with two-qubit gate operations [2, 3], long lived two-qubit entanglement [4–6], teleportation experiments [7, 8], and different sorts of multi-qubit entangled states [4, 9–11], the record for qubit-entanglement is currently presented in a 6-qubit cat state and a 8-qubit W-state [12, 13]. Future improvement is expected using the technique of segmented linear Paul traps which allow to shuttle ions from a "processor" unit to a "memory" section [14]. In such a quantum computer, strategies of quantum error correction will be critical for the successful operation. However, as a result, many additional ancilla qubits are required and a large fraction of the computational time will be consumed by shuttling ions between different segments. Detailed simulations [15] show that as much as 99% of the operating time would be spent with the transportation processes. The time required for the transport should be reduced such that the gate times are improved and decoherence processes are reduced.

Thus, we assume that the improvement of these transport processes is necessary. In recent experiments [12, 16], the shuttling has been carried out within the adiabatic limit, such that the time required for the transport by far exceeds the oscillation time of the ion in the potential. It is a common misbelief that this adiabatic transport is necessary to avoid the excitation of vibrational quanta. In this spirit, we investigate in this paper the optimization of fast and non-adiabatic transportation by applying classical optimal control theory. Our simulations allow to predict the time sequence of control voltages such that ion heating is suppressed.

* Corresponding author E-mail: kilian.singer@uni-ulm.de

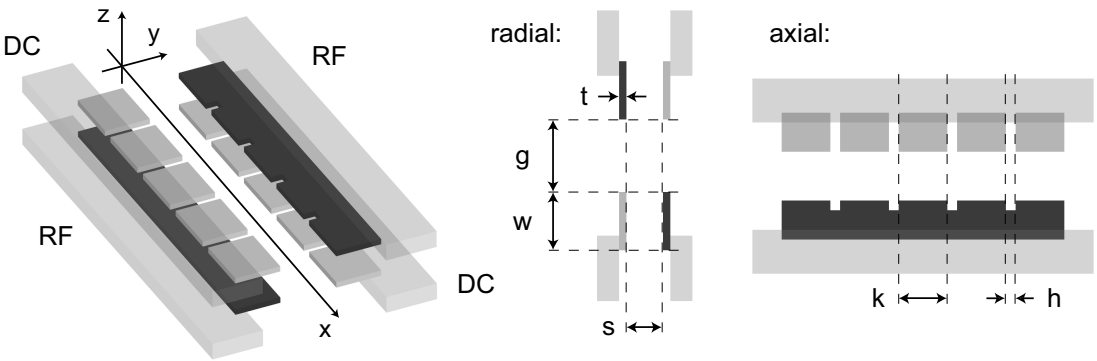

Fig. 1 Scheme of a two-layer micro structured segmented linear trap: The two electrode layers have a thickness t and are separated by the distance s. The length of the trapping electrodes is w, the radio frequency electrodes (RF) and the segmented electrodes (DC) are separated on each layer by the gap g (radial direction). The RF voltage is applied on two continuous electrodes (black) and the static voltages are applied on the segmented DC electrodes (gray). The DC electrode segments have the length k and are separated by a gap h. The symmetry axis is later denoted as the x- or axial direction.

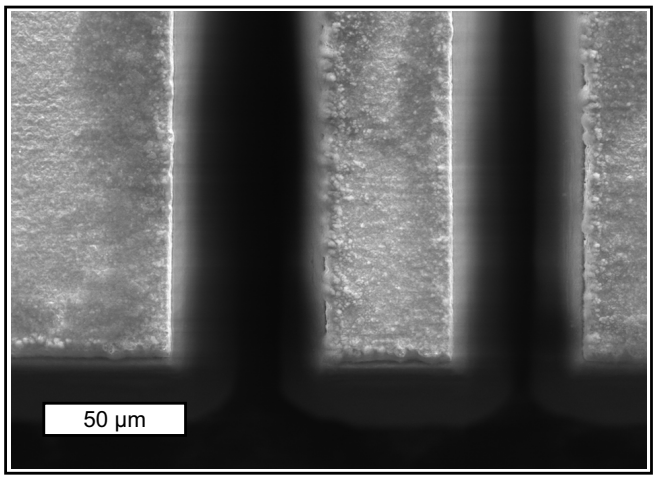

Fig. 2 Detail view on the trap chip, 5 µm gold plated alumina of 125 µm width cut by a fs-pulsed Ti:Sapphire laser. The scanning electron microscope picture shows several DC electrode segments of a single layer.

Certainly, non-optimized fast transport of qubit ions into the processor unit followed by sympathetic cooling of a different ion species [17, 18] would be an alternative strategy. However, the necessary cooling time would render the overall computational time even slower. First experiments show that the qubit coherence is maintained during a transport, but that the vibrational quantum state may typically not be well conserved after a fast shuttle of the ions. This impedes further qubit operations.

In the first section of this paper we start by numeric calculations of the electric trapping potential for ions and show how to optimize the geometry of a two-layer microstructured segmented trap [19, 20]. The same techniques may be applied for the optimization of planar ion traps [21–24]. In the second section we optimize the transport of a single ion between two regions and illustrate the application of optimal control theory [25]. Even though shuttling is fast, we can show that an optimized non-adiabatic transport does not lead to significant heating.

2 Optimization of a two-layer microstructured ion trap

The idea of segmented linear Paul traps has been proposed to realize a scalable quantum computer [14,26,27]. Typically, these trap structures are fabricated out of etched semiconductor structures [20] or gold plated insulators structured by microfabrication techniques [28]. Segmented traps come in various shapes and can be categorized by the number of electrode layers forming the trapping potential: Planar traps with one layer only, two-layer traps that are composed of two microstructured planar chips and traps with a higher number of electrode layers. In our discussion, we will focus on the two-layer geometry which is shown in Fig. 1. To illustrate the methods of fabrication, Fig. 2 gives an SEM picture of a gold plated laser cut alumina wafer. Here, with fs-laser ablation [29], the cuts are clean and show a spatial resolution of about 2µm. The DC-electrodes may be cut in form of "fingers" to reduce the insulating surface seen directly from the ion position. This reduces the influence of the possibly charged surfaces to the trap potential and has also been shown to reduce heating effects of the ion motion. Two structured wafers are assembled to form a two-layer trap geometry as shown in Fig. 1.

2.1 Design objectives

What are the optimal dimensions and aspect ratios in such an ion trap structure? What are the optimal electric trap parameters?

Radial configuration At first, we aim for a high secular trap frequency $\omega_{\text{sec}}/2\pi$, such that there is a tight dynamical confinement of the ions within the Lamb-Dicke regime. The confinement should typically reach frequencies of several MHz in the radial direction. The required radial frequencies should be achieved with moderate voltages on the electrodes of several hundreds volts. Therefore, the RF trap drive may not exceed the break-through voltage - a limitation which plays a significant role in the case of very small traps [20,21].

A second aspect is the anharmonicity of the radial trapping potential. From the fact that linear traps with optimized electrode shapes have been shown to load large crystals of ions [30], we would try to improve the loading rate by reducing non-harmonic contributions to the potential. Especially for larger q-values when the trap drive power is chosen relatively high, non-linear resonances have been observed [31]. This confirms that even small anharmonicities are relevant in the case of large crystals.

Axial configuration In order to maintain the linear appearance of the ion crystals, the axial trap frequencies have to be lower than the radial frequency. Nevertheless, the axial frequencies $\omega_{\text{ax}}/2\pi$ should exceed a few MHz. Then, cooling techniques are simpler [32], gate operations may be driven faster, and a faster adiabatic transport of ions between segments may be achieved. Ion transport between axial segments requires a fast temporal change of the trap control voltages on the order of several µs. This is accomplished by controlling the DC-electrode voltages by means of fast digital-to-analog converters (DAC) and would be technically much more involved for high voltages.[1]

Furthermore, single ions will have to be split off and merged to ion strings throughout the operation of a segmented ion trap quantum computer. The investigation of splitting and merging operations is not within the scope of this paper [33], however, it was pointed out that a highly non-harmonic axial potential improves this situation [34]; it implies certain geometrical ratios in the axial trap construction.

2.2 Operating mode and modeling of the segmented linear Paul trap

Linear Paul traps are characterized by a two-dimensional dynamical confinement in the radial direction (yz plane) and a static confinement in the axial direction (x-axis). The applied radio frequency $\omega_{\text{rf}}/2\pi$ to the RF electrodes (see Fig.1) generates a dynamical electric potential $\phi_{\text{rad}}(y, z, t)$ which leads to a strong confinement of single ions along the axial direction at the radio frequency node. Typically, the axial potential

[1] Therefore the geometry should also take into account the limited voltage range of the DACs.

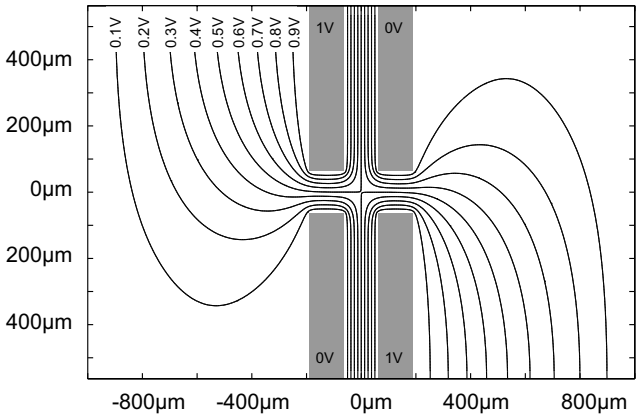

Fig. 3 Electric potential of the two-layer microstructure trap in radial direction (yz cross section). Ions are confined by a pseudo-potential on the x-axis. Here, the potential lines are normalized to a trap drive amplitude U_{rf} of 1V. In the central trapping region near the x-axis the electric potential may be approximated by a quadrupole potential as the radial harmonic pseudopotential for single ions.

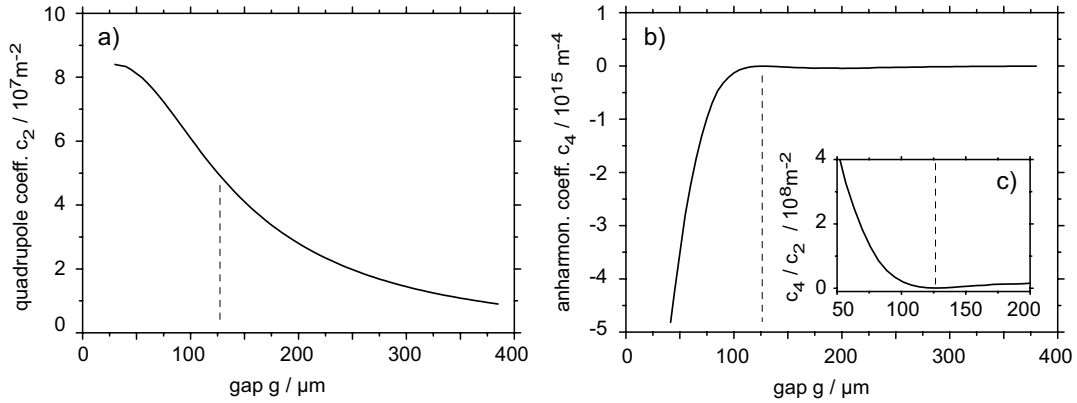

Fig. 4 a) Numerical simulation of the trap stiffness c_2 in radial direction as a function of the slit width. For a slit width of 126 µm we estimate a value of $5.5{\cdot}10^7\text{m}^{-2}$ which corresponds to a radial frequency of $\omega_{\text{rad}}/2\pi = 5$MHz. b) Dependence of the fourth order parameter c_4 to the slit width g. The dashed line near 126 µm indicates the optimization result. c) The normalized hexapole coefficient c_4 normalized by the quadrupole coefficient c_2 indicates the descreased loss of the trap drive power.

$\phi_{\text{ax}}(x,t)$ formed by the quasistatic voltages applied to the segmented DC electrodes is weaker than the radial confinement to support a robust alignment of the linear ion string. The shape of this axial potential depends on the geometry of the segmented DC electrodes. The time-dependent variation of the DC control voltages allows to transport ions in the axial direction without micromotion. We separate the numerical optimization of the linear Paul trap into a radial and axial calculation – first, the radial geometry configuration is optimized for strong confinement in the RF node, then the axial electrode geometry is calculated based on the radial geometry.

The lowest-order approximation of the dynamical trap potential $\phi_{\text{rad}}(y,z,t)$ in radial direction is similar to that of a quadrupole mass filter [35]. The geometric factor c_2 describes the quadrupole potential strength in both radial directions for a symmetric radial electrode geometry:

$$\phi_{\text{rad}}(y,z,t) = c_2/2\,(y^2 - z^2)\,(U_{\text{dc}} + U_{\text{rf}} \cdot \cos(\omega_{\text{rf}}\,t)) \tag{1}$$

An ion trajectory is described as a superposition of a harmonic secular motion at frequency $\omega_{\text{sec}} = \omega_{\text{rf}}/2\,\sqrt{a + q^2/2}$ (lowest order approximation) and the superposed micromotion at the radio frequency ω_{rf}. The frequency of the secular motion is characterized by the dimensionless stability parameters a and q of the radial motion [36] which depends on mass m and charge e of the ion, the RF amplitude U_{rf} applied to

the RF electrodes and the static voltages U_{dc} applied to the segmented electrodes of the trap:

$$a = \frac{4e\,U_{\mathrm{dc}}}{m\,\omega_{\mathrm{rf}}^2}\;c_2 \quad , \qquad q = \frac{2e\,U_{\mathrm{rf}}}{m\,\omega_{\mathrm{rf}}^2}\;c_2 \tag{2}$$

A two-dimensional domain of the stability parameters a and q defines a region of stable trajectories as solutions of the classical equations of motion[2]. In general, the electrode configurations result in an electric potential that may be expanded in spherical multipole components, where the quadrupole contribution c_2 represents the dominating part for reasonable Paul trap geometry; the hexapole contribution c_4 contributes mainly to the non-harmonic part.

The quadrupole approximation of the confining potential is inaccurate if the electrode shapes deviate strongly from the ideal hyperbolic form. As a result, anharmonicities and coupling terms appear inside the stability region [31]. As the radio frequency voltage is portioned to various higher order terms and not only to the quadrupole contribution of the potential a loss of the trap stiffness c_2 is observed (Fig. 4). For simplicity we idealize U_{dc} as zero and characterize the anharmonicity of the pseudopotential in radial direction along the two radial principal axes, here denoted by a radial coordinate $r(y,z)$, by the leading terms of the following polynomial expansion:

$$\phi_{\mathrm{rad}}(r(y,z),t) \propto \sum_n c_n\; r^n \tag{3}$$

Because of the radial electrode symmetry the odd-numbered terms $c_1, c_3, \ldots$ are negligible and the potential offset c_0 is irrelevant. The optimization of the radial trap potential leads to a suppression of the higher order potential contribution, such that the hexapole term c_4 as the leading non-harmonic contribution is small.

Based on the geometry for an optimized radial confinement the axial static trap potential along the symmetry axis x can be analogously expanded,

$$\phi_{\mathrm{x}}(x,t) \propto \sum_n d_n\; x^n. \tag{4}$$

The axial potential properties are determined by the segmented electrode geometry, especially the axial width of the individual electrode segments. An optimal axial confinement of the ion requires a maximum quadratic term d_2. The transport of a single ion between axial segments is facilitated if the potentials from adjacent segments exhibit a large overlap. For the splitting operation of an aligned two-ion crystal into single ions in independent axial potentials, Steane et al. [34] suggest a potential shape with a maximum quartic term d_4 and minor quadratic contribution d_2.

Relevant parameters of various linear ion traps are summarized in Table 1. The Aarhus hexapole design with endcaps [37] and the Innsbruck blade design [38] show a traditional macroscopic approach of mm-size linear trap design without segmentation of the control electrodes. The Michigan trap designs, the microstructured three-layer trap [39] and the semiconductor two-layer trap [40], represent the progress in the miniaturization of linear ion traps and the segmentation of the control electrodes for the transport of single ions and the splitting of ion crystals.

2.3 Optimization of the radial potential

In the first step we optimize the radial confinement of the trap. The width of the slit is varied and the electric potential is calculated, see Fig. 3. The distance of the two layers is fixed to the thickness of a commercial alumina wafer (125 µm) which acts as a spacer. Then a variable parameter is the width g of the lateral laser cut in the trap chips, respectively the distance between the RF and the DC-electrodes of the trap chips. We find that the radial confinement increases with decreasing slit width g, see Fig. 4. Interestingly, for this

[2] We discuss the optimization in the so-called lowest stability region including $a = 0$ and $q \leq 0.9$

Table 1 Trap design parameters of several types of linear ion traps: The geometric trap R size given by the minimal distance between ion position and electrode surface, the quadratic geometry factor c_2 of the radial cross section describes the magnitude of the radial confinement at the given electrode voltage, the trap drive frequency $\omega_{\text{rf}}/2\pi$ together with the trap drive voltage U_{rf} and the RF stability parameter q results in the radial motional frequency $\omega_{\text{rad}}/2\pi$. For comparison the axial motional frequency $\omega_{\text{ax}}/2\pi$ is shown. The trap depth Δ summarizes the confinement of a single ion.

		R [µm]	c_2 [$1/\text{m}^2$]	$\omega_{\text{rf}}/2\pi$ [MHz]	U_{rf} [V]	q	$\omega_{\text{rad}}/2\pi$ [MHz]	$\omega_{\text{ax}}/2\pi$ [MHz]	Δ [meV]
Aarhus [37]	$^{24}\text{Mg}^+$	1750	$1.6 \cdot 10^5$	4.2	$2 \cdot 50 \cdots 2 \cdot 150$	$0.2 \cdots 0.6$	$0.3 \cdots 0.8$	≤ 0.4	$\leq 10^5$
Innsbruck [38]	$^{40}\text{Ca}^+$	800	$3.9 \cdot 10^6$	23.5	700	0.6	5.0	1.0	1000
Michigan [39]	$^{112}\text{Cd}^+$	100	$2.2 \cdot 10^7$	48.0		0.3	5.0	2.5	
Simulation	$^{40}\text{Ca}^+$	89	$5.3 \cdot 10^7$	50.0	120	0.3	5.0	2.5	300
Michigan [40]	$^{112}\text{Cd}^+$	30	$4.7 \cdot 10^8$	15.9	8	0.6	4.3	1.0	80

geometry, the radial potential is almost harmonic since the fourth order parameter c_4 is nearly vanishing. For a width of 126 µm the radial frequency of $\omega_{\text{rad}}/2\pi = 5$ MHz is reached for a singly charged $^{40}Ca^+$ ion with a peak RF voltage of 120 V at 50 MHz.

2.4 Optimization of the axial potential

The optimization of the axial potential determines the performance of the fast ion transport. Additional requirements are a deep axial potential even with moderate DC control voltages and the capability of the segments to split a two-ion crystal into two single ions trapped independently in distinct potential minima.

In a first step we investigate the maximization of the axial trap frequency ω_{ax} as a function of the segment width k and the cut width h, see Fig.1. The numerical three-dimensional electric potential simulation is depicted in Fig. 6 which shows the expected result. For a large width of the segments, the potential is expected to be shallow, and for a very short width the electric potential falls rapidly off from the electrode tips such that again, a weak confinement is found. The maximum axial trap frequency is reached for a segment width $k_{\text{opt}} \simeq 70$ µm, a gap between DC and RF electrode g= 126 µm between DC and RF electrode and a cut width of h= 30 µm. Changing the size of the segment width by 50% results only in a 20% variation of d_2 which is easily compensated by the DC voltage.

The trapping of single ions and transport require a different electrode configuration. For the transport problem, it is important that the potentials generated by adjacent DC segments exhibit a large spatial overlap (see Fig. 5). To achieve both ideal trapping and transport conditions we split each electrode into two parts (b). For trapping we bias two neighboring electrodes with an equal voltage in order to obtain a larger "effective" electrode. Due to the smaller segmentation a better overlap of the individual potentials is provided during transport. As the ion is displaced during the transport process we expect that the anharmonic terms $d_4, d_5, \ldots$ of the potential will cause heating, see Sect. 3.5. Therefore we have determined the optimal effective segment width such that the d_4 term is minimized. The results are shown in Fig. 6.

In the following, we will use the simplified transport scheme in Fig. 5 (c) with one start and one target electrode only and investigate the necessary time dependence of both DC segment control voltages.

3 Open loop control of ion transport

After the optimization of all geometric trap parameters we now focus on the optimization of the time dependent trap control voltages which are applied on the DC segments in order to transport the ion: Our goal will be to decrease the time required for the transport far below the limit of adiabaticity, such that the transport is finished within a single oscillation period only, with the constraint to avoid vibrational excitation. To a

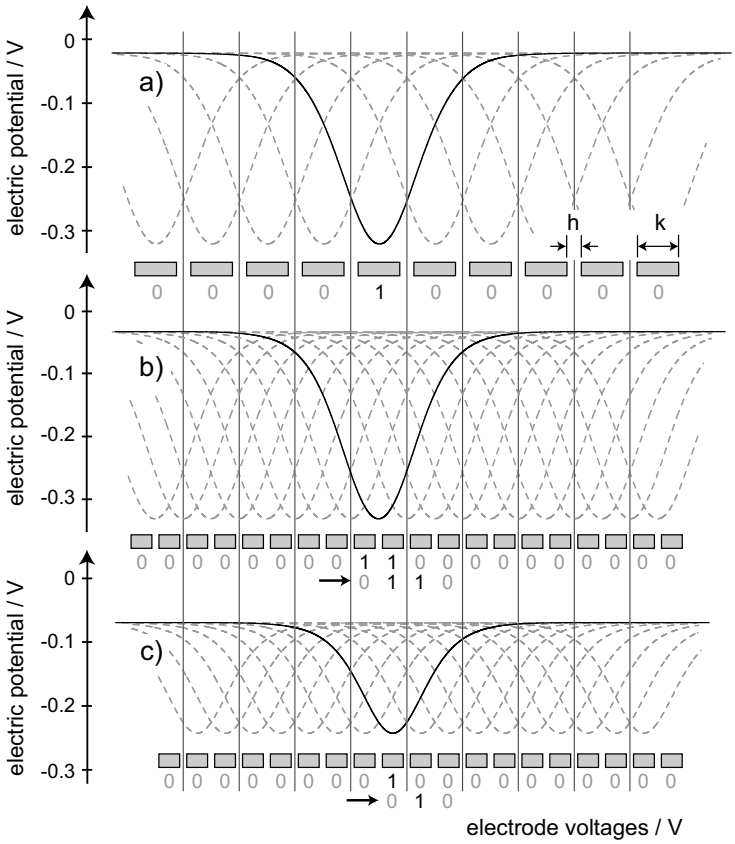

Fig. 5 Numerical calculation of the axial electric potentials ϕ_{ax}, all cases (a) to (c) for the optimized radial slit width of $g = 126$ µm. a) DC segments with a width of $k = 90$ µm and gaps between axial electrodes of $h = 30$ µm result in a maximal d_2 coefficient. The potential of the adjacent electrode is plotted and shows only partial overlap (dashed gray). b) Optimized transport scheme: The DC electrodes are divided into equal parts with $k = 45$ µm and $h = 15$ µm. If both electrodes are at the same voltage of 1V, the potential is nearly identical to the optimized case (a). For transporting an ion, the potential minimum is shifted by changing the voltages from ..0/0/1/1/0/0.. $\rightarrow$ ..0/0/0/1/1/0.. continuously. The axial potentials exhibit a large overlap which improves the transport of the ions. c) Simplified transport scheme: Axial potential for DC segments with $k = 45$ µm and $h = 15$ µm. Now, only a single segment is at 1 V. For transporting the voltages are changed from ..0/1/0/0/.. $\rightarrow$ ..0/0/1/0/...

good approximation the radial ion confinement does not influence the axial transport between two segments as the ion is moving along the central RF-node with negligible micromotion. Note, that our calculation takes into account two axial segments but may be adapted to a larger number of segments, see Fig. 5 (c). The potential which we use for the optimization of the ion transport is the result of a boundary element calculation, see appendix A. In order to transport the ion, the potential minimum is shifted by changing the DC control voltages $u_i(t)$. Intuitively, we estimate that a smooth acceleration and a smooth deceleration of the ion is advantageous. Searching for the precise shape of the segment control non-adiabatic heating due to fast transport has to be minimized.

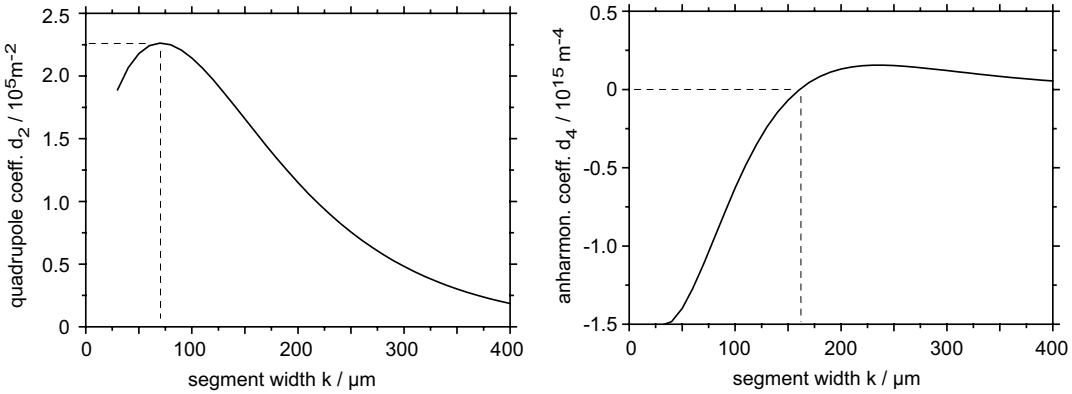

Fig. 6 a) Numerical simulation of the axial trap stiffness d_2 as a function of the segment width k with $h =$ 30 µm. b) Dependence of the fourth order parameter d_4, the dashed line near k =160 µm indicates the zero crossing.

3.1 Non-adiabatic heating sources

For a transport duration approaching the timescale given by the axial trap frequency, the following non-adiabatic effects are expected to occur:

1. *Classical displacement error:* The ion cannot adiabatically follow the potential minimum and starts oscillating, such that it possesses excess energy after the transport process. This behavior may be understood classically. In the quantum picture it corresponds to the buildup of a nonvanishing displacement α during transport.
2. *Wavepacket dispersion heating:* With a spatial extension of about 10 to 20 nm, the undisplaced wavefunction hardly senses any anharmonicity in an electric potential that is generated by 50 to 100 µm sized electrode structures. However, during the transport the wavepacket undergoes significant excursions of a few µm out of the minimum of the potential. Here, exposed to higher anharmonic d_4 contributions, the shape of the ion wavepacket disperses which results in vibrational excitation.
3. *Parametric heating:* As the control voltages are changed, the harmonic frequency ω of the instantaneous potential is temporarily varying. If the width of the wavepacket can not follow the variation of $\omega(t)$ adiabatically, parametric heating to higher vibrational states will occur.

3.2 Overview of the applied optimization strategies

In the following Sect. 3.3 we minimize the classical displacement error by applying the optimal control method. For the optimization of this entirely classical error source we need to optimize the ion's classical trajectory such that a cost function – weighting the ion's phase space displacement after the transport – is minimized. The solution obtained by the optimal control algorithm does not show considerable heating by wavepacket dispersion. However, we find a significant contribution of parametric heating. A first guess would be to include an additional term in the cost function to prevent parametric heating, involving time derivatives of the control fields.

As this approach fails due to implementational difficulties, we suppress parametric heating by an appropriate initial guess which keeps the trap frequency perfectly constant. This is achieved by a variable transformation from $u_{1,2}(t)$ to new parameters that allow to decouple the strength of the potential and its minimum position. Starting now the optimal control method yields a solution that reduces the displacement

error. Since the control parameters are only slightly modified by the optimization algorithm, the parametric heating and also the wavepacket dispersion heating are negligible.

We conclude that in our case, the choice of variables that decouple the essential optimization parameters [41,42] and a well suited initial guess function are helpful and maybe critical for the success of the optimal control method.

3.3 The optimal control method

This section will give an introduction to optimal control theory applied to single ion transport. We use the method derived from a variational principle with unbounded controls and fixed final time [43]. We consider the dynamics of a singly charged single $^{40}Ca^{+}$ ion confined in a segmented linear Paul trap. We assume that the ion is laser cooled to its motional ground state [3] pertaining to the axial degree of freedom. Neglecting the radial motion, the motional state of a trapped ion is classically represented by a coordinate vector $\vec{\xi}(t) = (x, v)^T$ in a two dimensional phase space.

The equation of motion under consideration of two uniform electrode segments with arbitrary voltages applied on them, reads

$$\dot{\vec{\xi}} = \vec{a}(\vec{\xi}, \{u_i\}) = \begin{pmatrix} v \\ -\frac{1}{m}\sum_i \frac{\partial V_i(x)}{\partial x} u_i(t) \end{pmatrix}. \tag{5}$$

Here, the index i runs over the two electrodes and $V_i(x)$ are the normalized electrostatic potentials at electrode i. Eq. (5) then holds for arbitrary electrode voltages due to the linearity of the Laplace equation. Our goal is now to find time-dependent control voltages $u_i(t)$ that move the ion from the center of electrode 1 to the center of electrode 2. We desire to have the ion at rest after the transport process. The performance of a given control field is judged by the cost function

$$h(\vec{\xi}(t_f)) = \alpha\,(x(t_f) - x_f)^2 + \beta\, v(t_f)^2, \tag{6}$$

which is a measure of the phase space displacement at the final time t_f. α and β weight the contributions relative to each other. Taking Eq. (5) as a constraint for all times t, we obtain the cost functional

$$J(\vec{\xi}, \vec{\xi}_p, \{u_i\}) = \int_{t_0}^{t_f} \frac{\partial h}{\partial \vec{\xi}} \cdot \dot{\vec{\xi}} + \vec{\xi}_p \cdot \left(\vec{a}(\vec{\xi}, \{u_i\}) - \dot{\vec{\xi}} \right) dt \tag{7}$$

where we have introduced the costate vector $\xi_p = \left(x_p, v_p\right)^T$ as a Lagrange multiplier in order to guarantee that the optimization result obeys the equation of motion Eq. (5). The time dependence of all variables has been dropped in the notation. For an optimal control field, $\delta J = 0$ has to hold, therefore the variational derivatives with respect to $\vec{\xi}, \vec{\xi}_p$ and $\vec{u}$ have to vanish. The derivative with respect to $\vec{\xi}_p$ restores the equations of motion Eq. (5) for the state vector, the derivative with respect to $\vec{\xi}$ yields equations of motion for the costate vector:

$$\begin{aligned} \dot{\vec{\xi}}_p &= -\frac{\partial \vec{a}}{\partial \vec{\xi}} \cdot \vec{\xi}_p \Rightarrow \\ \dot{x}_p &= v_p \frac{1}{m} \sum_i \frac{\partial^2 V_i(x)}{\partial x^2} u_i \\ \dot{v}_p &= -x_p. \end{aligned} \tag{8}$$

Variation of J with respect to the control field leads to an additional algebraic equation:

$$\frac{\partial \vec{a}}{\partial u_i} \cdot \vec{\xi}_p = 0 \Rightarrow -\frac{1}{m} \frac{\partial V_i(x)}{\partial x} v_p = 0. \tag{9}$$

[3] The calculation is valid also for thermal and coherent states with modest excitation.

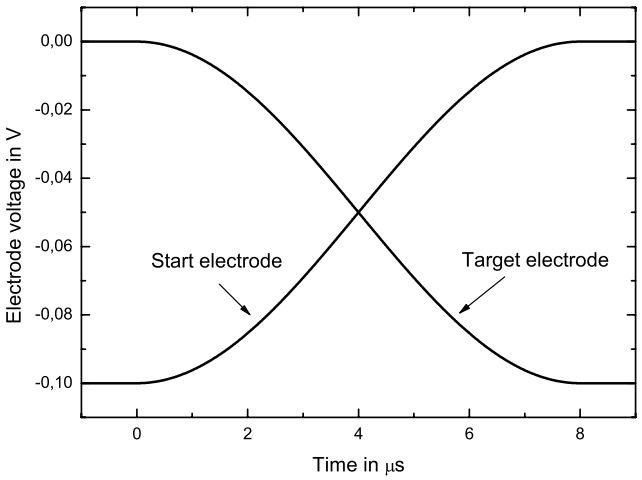

Fig. 7 Initial guess for the control voltages, corresponding to Eq. (13).

The boundary condition for $\vec{\xi}_p$ is derived by variation with respect to the final state:

$$\left| \frac{\partial h}{\partial \vec{\xi}} \right|_{t_f} = 0. \tag{10}$$

If we let the ion start at rest in the potential well pertaining to the first electrode, the set of boundary conditions for the state and costate vector reads

$$\begin{aligned} x(t_0) &= 0 \\ v(t_0) &= 0 \\ x_p(t_f) &= 2\,(x - x_f) \\ v_p(t_f) &= 2\,v. \end{aligned} \tag{11}$$

Eqs. (5), (8) and (11) together with (9) represent a system of coupled ordinary nonlinear differential equations with split boundary conditions, i.e. for two of the variables, initial conditions are given whereas for the other two, the values at the final time are specified. This makes a straightforward numerical integration impossible. The system is therefore solved in an iterative manner by means of a gradient search method. The scheme of this steepest descent algorithm is as follows:

1. Choose an initial guess for the control field $u_i(t)$.
2. Propagate x and v from $t = t_0$ to $t = t_f$ while using $u_i(t)$ in the corresponding equations of motion. At each time step, save the value of $x(t)$.
3. Determine $x_p(t_f)$ and $v_p(t_f)$ according to (11).
4. Propagate x_p and v_p backwards in time from $t = t_f$ to $t = t_0$. At each time step, save the value of $v_p(t)$.
5. For each time step, update the control field according to

$$u_i^{new}(t) = u_i^{old}(t) + \tau\, v_p\, \frac{1}{m} \frac{\partial V_1(x)}{\partial x} \tag{12}$$

6. Repeat steps 2 to 5 until the specified threshold fidelity is reached.

In Eq. (12), the gradient search step width τ is simply chosen by trial and error. If it is too small, the algorithm converges too slowly, if it is too large, the algorithm starts to oscillate. The values of α and β in Eq. (6) are determined based on experience. For the data presented in the following section, these values are $\alpha = 10,\ \ \beta = 1$ and $\tau = 5 \cdot 10^{-8}$. The algorithm converged after about 200 iterations.

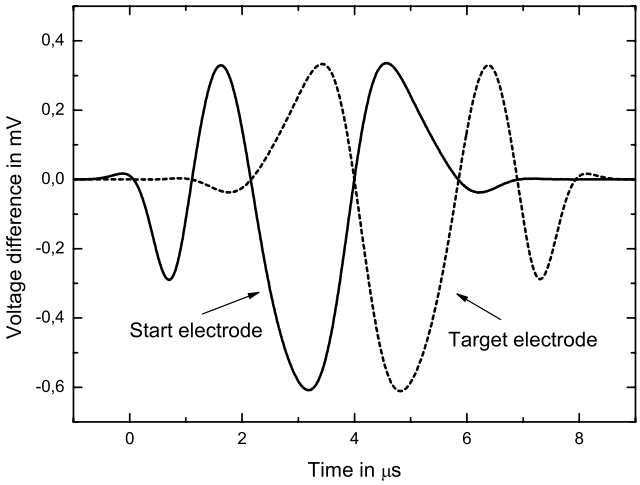

Fig. 8 Optimized control voltages given in terms of change with respect to the initial guess values. The solid curve indicates the voltage $u_1(t)$ at the start electrode, the dashed one the voltage $u_2(t)$ at the destination electrode.

3.4 Optimization results

For the initial guess the control field is chosen as follows:

$$u_0^{(0)}(t) = \begin{cases} V_0 & \text{for } t \leq 0 \\ V_0 \ \sin^2(\frac{\pi t}{2\Delta t}) & \text{for } 0 < t \leq \Delta t \\ 0 & \text{for } t > \Delta t \end{cases}$$

$$u_1^{(1)}(t) = V_0 - u_0^{(0)}(t) \tag{13}$$

This provides on the one hand a smooth and symmetric acceleration and deceleration of the ion, on the other hand the potential minimum exactly coincides with the desired positions at the initial and final times. In principle, other initial guess voltages like Gaussian flanks can be used as well. The reference voltage is $V_0 = -0.1V$, corresponding to $\omega \approx 2\pi \cdot 0.5$ MHz in the initial and final potential wells. The switching time is set to $\Delta t = 8.0$ µs, the total time interval runs from -1.0 µs to 9.0 µs.

3.5 Ion heating due to anharmonic dispersion

Quantum mechanically we describe the system with a Hamiltonian operator pertaining to a time-dependent harmonic oscillator with an anharmonic perturbation:

$$H_0(t) = \frac{\hat{p}^2}{2m} + \frac{m\,\omega(t)^2}{2}(\hat{x} - x_0(t))^2 + \kappa(t)(\hat{x} - x_0)^4. \tag{14}$$

Without temporal variation of ω and the anharmonic part[4] of the potential, the solution of the time-dependent Schrödinger equation is simply given by a coherent state $|\alpha(t)\rangle$, where the displacement parameter $\alpha(t)$ can be inferred from the classical trajectory. Anharmonic dispersion of a wavepacket occurs at a timescale given by $T_{\rm rev}/(\Delta n)^2$ [44], with the revival time

$$T_{\rm rev} = 2h\left(\frac{d^2E_n}{dn^2}\right)^{-1} \tag{15}$$

and the spread over the vibrational levels $\Delta n = \alpha(t)$. The shift of the energy levels E_n induced by the anharmonic contribution causes a finite dispersion time and can be calculated in first order stationary

[4] In contrast to d_4, $\kappa(t)$ is given by expanding the potential around the instantaneous potential minimum.

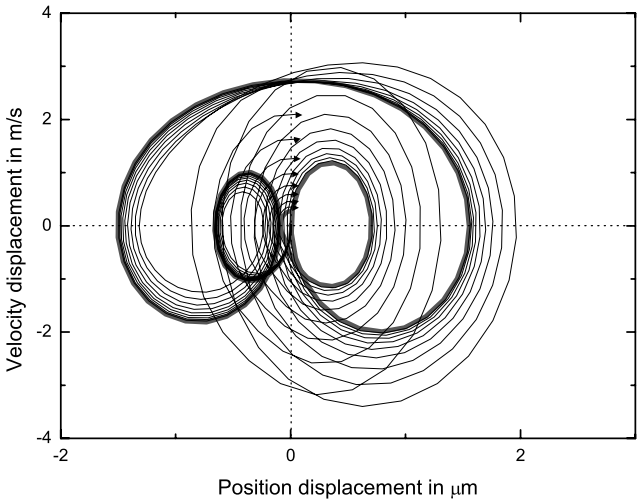

Fig. 9 (online colour at: www.fp-journal.org) Phase space trajectories in the frame co-moving with the potential minimum. The figure shows the trajectories pertaining to iterations 0, 10 , ..., 100. At iteration 100, the ion arrives close to the origin. Note that the trajectory tends to be symmetrized by the optimization algorithm.

perturbation theory:

$$\Delta E_n(t) = \frac{5}{4}\frac{\hbar^2\kappa(t)}{m^2\omega(t)^2}n^2. \tag{16}$$

We now define a generalized dispersion parameter

$$\int_{t_0}^{t_f} dt \frac{\Delta n^2}{T_{\rm rev}} = \frac{5\ \hbar}{4\pi\ m^2}\int_{t_0}^{t_f} dt \frac{\kappa(t)|\alpha(t)|^2}{\omega(t)^2}. \tag{17}$$

If this parameter is sufficiently small, anharmonic dispersion will not contribute to heating.

3.6 Quantum mechanical estimate of non-adiabatic parametric heating

We now check if the width of the wavepacket adiabatically follows the harmonic frequency $\omega(t)$. The adiabatic theorem states that if

$$\hbar\langle\phi_m(t)|\dot{\phi}_n(t)\rangle \ll |E_n(t) - E_m(t)| \tag{18}$$

is fulfilled, transitions between eigenstates can be neglected. The parametric time dependence of the eigenstates states in Eq. (18) is the implicit time dependence via $\omega(t)$. We find the following nonvanishing matrix elements:

$$\begin{aligned}\langle\phi_{n+1}|\phi_n\rangle &= \frac{\dot{\omega}}{\sqrt{2\pi^3}\omega}n\sqrt{n+1}\\ \langle\phi_{n+2}|\phi_n\rangle &= \frac{\dot{\omega}}{4\omega}\sqrt{(n+1)(n+2)}\end{aligned} \tag{19}$$

and similar expressions for $m = n-1, n-2$. Thus, parametric heating can be neglected if

$$n^{3/2}\ \frac{\dot{\omega}}{\omega^2} \ll 1. \tag{20}$$

Numerical evaluation of the matrix elements yields the result that the adiabatic following condition is fulfilled for $n = 0$, but is clearly violated for the high n occurring for large excursion of the wavepacket, for example $\bar{n} \approx 2000$ for $\Delta x = 1$ μm at a transport time of 10 μs, see Fig. 10.

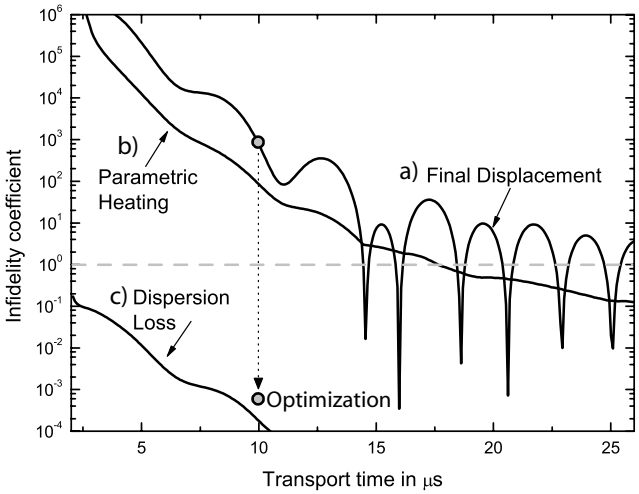

Fig. 10 Non-optimized transport, heating effects, and optimization result: Indicated is the excess energy as a function to transport time, if the initial guess function is used for the transport. The curve (a) describes the energy at the final time in vibrational quanta. The approximate zeros occur when the deceleration of the potential minimum coincides with the ion oscillation. Curve (b) displays the maximum non-adiabaticity parameter Eq. (20) for parametric heating and the (c) the anharmonic dispersion loss parameter from Eq. (17). The grey dashed horizontal line indicates a heating of one phonon and the borderline to non-adiabatic behavior in curve (b). The optimization algorithm decreases the excess displacement by more than 6 orders of magnitude. The circles indicate the squared phase space displacement for the guess function and the final optimized control voltages.

3.7 Improved initial guess function and ultra-fast transport

We therefore have to refine our optimization strategy: As can be seen in Fig. 8, the control voltages changes are symmetric, which indicates that one control degree of freedom can be sacrificed in order to keep $\omega(t)$ constant. This is achieved as follows: The initial guess voltages Eq. (13) are normalized to a constant ω before the optimization. The optimization process then leads to variations in $\omega(t)$ that are negligibly small - typically leading to maximum values of $\dot{\omega}/\omega^2$ on the order of 10^{-5} such that according to Eq.(20) the adiabatic theorem is fulfilled even after the optimization algorithm has cured the classical phase space displacement heating. This is in strong contrast to the unconstrained, previous guess function, where we obtain $\dot{\omega}/\omega^2 \simeq 10^{-2}$. It should be noted that parametric heating can be completely suppressed as well for optimized control voltages. This can be achieved by changing the set of control parameters to $\tilde{u}_1 = u_1 + u_2$ and $\tilde{u}_2 = u_1/\tilde{u}_1$. The new parameter $\tilde{u}_2$ is now directly related to the instantaneous potential minimum x_0. If only $\tilde{u}_2$ is incorporated in the optimization process, $\tilde{u}_1$ can be readjusted at each step to keep ω constant.

The optimization results for the improved initial guess voltages are shown in Fig. 12. The transport time could now be reduced to 5 μs which corresponds to roughly two oscillation periods. For the improved guess function the wave package dispersion appears now as the dominant heating source. This process could be suppressed either by further geometric optimization of the trap segments or by including a corresponding additional term into the cost function of the optimization routine.

3.8 Discussion of the open-loop result

Our optimization results indicate that unwanted heating during ion transport can be suppressed by many orders of magnitude by the application of appropriate time-dependent control voltages. Technically, one would achieve this using a fast high-resolution digital-to-analog converter (DAC) with subsequent scaling

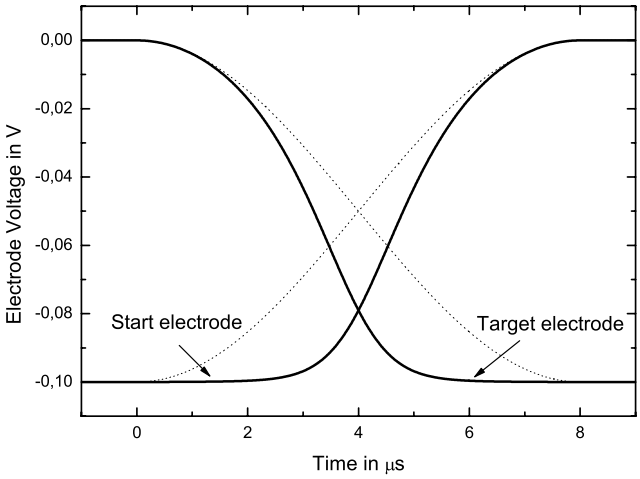

Fig. 11 Initial guess voltages normalized to keep trap frequency constant. The old initial guess voltages are indicated as dashed curves. Note that the dynamics of the potential minimum is unaffected by the normalization.

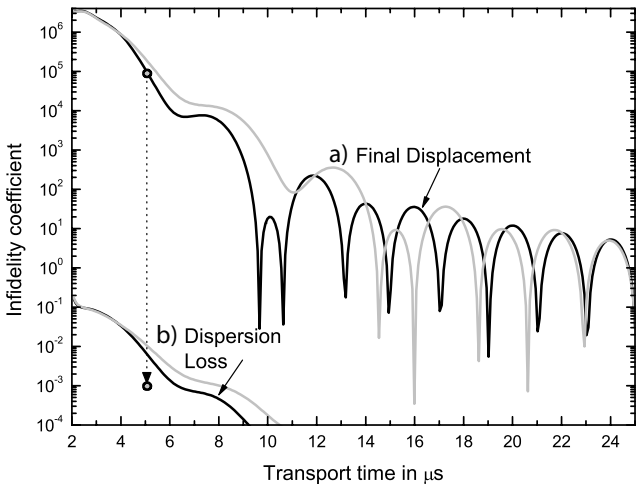

Fig. 12 Nonadiabatic effects versus transport time for the improved initial guess voltages. Here, only the (a) excess displacement and the (b) dispersion parameter are shown, parametric heating is not relevant anymore. The values for the old initial guess voltages are indicated in grey. The improved initial guess allows for successfull optimization at a transport time of 5 μs and an optimization of about eight orders of magnitude in classical phase space displacement. Now, with a few μs transport, anharmonic dispersion becomes the predominant heating source.

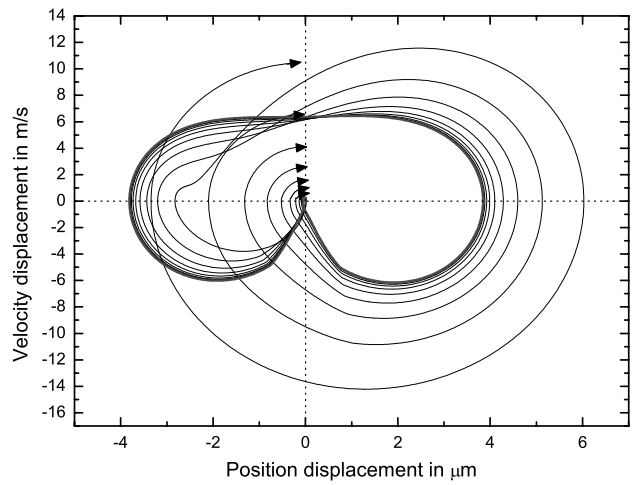

Fig. 13 (online colour at: www.fp-journal.org) Phase space trajectories in the frame co-moving with the potential minimum for the improved initial guess voltages. The optimization is now carried out for transport time of only 5 μs corresponding to about two oscillation periods in the harmonic trap potential. The thin lines indicate the optimization progress and the fat line shows the final result after 100 iterations. Again, the optimization routine symmetrized the trajectory.

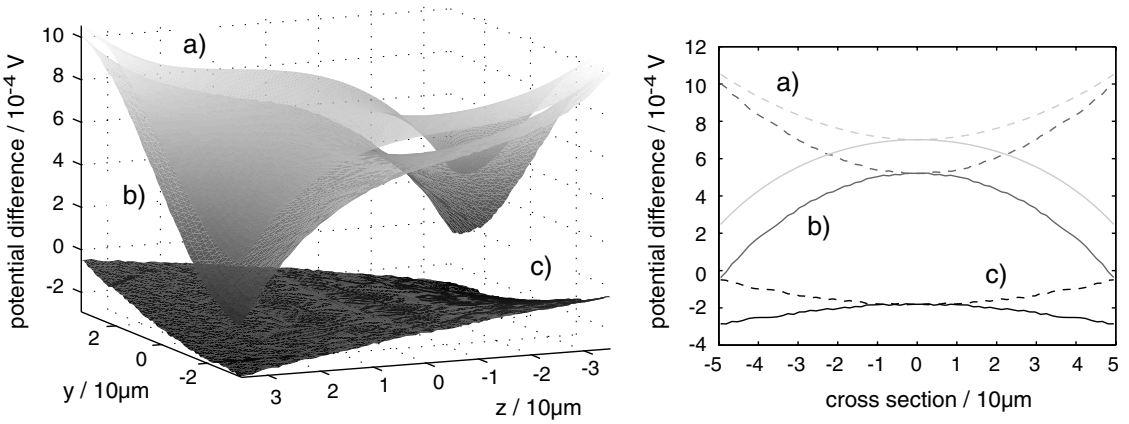

Fig. 14 a) Numeric result obtained by FEMLAB substracted from the result of BEM [55], b) FEMLAB – CPO, c) CPO – BEM [55]. The left graph shows a 2D potential surface plot in the y-z plane. The right graph shows a line plot in the same plane in the direction of the two diagonal directions.

to the required voltage range. The small correction voltages obtained from the optimization algorithm might represent a problem, however a 16 bit DAC with an appropriate scaling circuit would allow for a discretization step of roughly 1.5 µV for a maximum voltage change of 0.1V. We have also checked the robustness of the control field solutions against noise by calculating the trajectories with white noise of variable level added on the voltages. We found a quadratic dependence of the excess displacement on the noise level. The deviation of the final displacement from the noise-free case was negligibly small at a noise level of 20 µV. Experimental values for non-adiabatic heating effects in ion transport are given in [16]. The comparison with our theoretical values is hampered by the fact that these measurements have carried out at higher axial trap frequency and the lighter ion species $^9Be^+$, but over a much longer transport distance of 1.2 mm. However, low heating rates were obtained in those experiments only if the transport duration corresponds to a relatively large number of about $\simeq$ 100 of trap periods, whereas in our case, a transport within only *two trap periods* was simulated.

4 Outlook

The optimization of ion transport beyond the speed limits given by the anharmonic terms of the axial trapping potentials and parametric heating would be most efficient and accurate if a full quantum mechanical equation of motion was employed. Quantum mechanical optimal control methods are based on the same variational principle as presented here for a classical problem, with the only difference that the terms in the penalty functional are functionals on Hilbert space. Algorithms for quantum mechanical optimal control are well developed and were applied to variety of different problems [41,45]. In our case however, the application of quantum mechanical optimal control was not yet possible for simply a technical reason: The iterative solution via repeated solution of Schrödinger equation over distances on the order of 200 µm and time spans on the order of 20 µs takes too much computational effort, even with highly efficient methods like the Fourier Grid Hamiltonian combined with the Chebyshev propagator technique [46]. On the other hand, we have seen that for the typical electric potentials of segmented Paul traps, the possibility to exert *quantum* control on the system is very restricted since the wavefunction of the ion mainly senses a harmonic potential. The classical approach is therefore well suited to the problem.

In future work, we will investigate whether quantum control could be exerted during short time spans when the ion is displaced from the potential minimum and therefore senses anharmonic contributions to the potential. Extended Gaussian wave packet dynamics [47] could be used to take anharmonic terms efficiently

into account. Thus, the application of quantum mechanical optimal control methods also opens new possibilities, for example the control voltages could be used to devise new schemes for quantum computational gates. In this case, the target wave function for the optimization routine could be the first excited motional state or even a superposition of different motional Fock states. To fulfill this aim, anharmonic contributions to the trapping potentials are crucial.

Open loop optimal control methods will also be applied to the splitting of two ions [33]. With this problem the benefit of going beyond the adiabatic limit will be even more promising. In an adiabatic manner the splitting is initiated by lowering the steepness of the potential in order to increase the separation of the two ions due to their mutual repulsion. This decreases the trapping frequency and as a consequence the speed of the procedure has to be decreased in order to stay adiabatic.

Open loop optimal control has proved to be successful for the optimization of short broadband RF pulses in NMR experiments [48]. In a similar manner in ion trap based quantum computing tailored, light pulses can speed up and improve manipulation of the ions [49,50]. In cases where analytical solution to the control problem is not available open loop optimal control methods could be applied to get optimized light pulses or electrostatic field configurations for multi ion gate operations and entangled state preparation.

Another promising strategy that could be employed to avoid heating during ion transport is the closed loop control technique. Here, the experimental results are fed back into e.g. an evolutionary algorithm to obtain improved values of the control parameters. The heating rate can be measured by comparing the strengths of the red and blue motional sidebands after the transport process [51]. The key problem for applying closed loop control to ion transport lies in finding an appropriate parametrization of the control voltages in order to keep the parameter space small.

This technique may be applied equally well to the problem of separation of two ions from one common potential into two independent sections of the linear trap.

This work has merely started to apply the optimal control theory for ion trap based quantum computing. Not only the motion of ions between trap segments, but the entire process including shaped laser pulses [49] and motional quantum state engineering might be improved with this technique.

Acknowledgements We acknowledge support by the European commission, the Deutsche Forschungsgemeinschaft and by the Landesstiftung Baden-Württemberg within the frameworks "quantum highway A8" and "atomics". We thank D. J. Tannor and T. Calarco for stimulating discussions.

A Comparison of our boundary-element-package with commercial software

Accurate values of the electrostatic potentials are of paramount importance for the determination of the harmonic and the anharmonic terms of the trapping potentials. An adequate choice of a numerical solving method is the Boundary Element Method (BEM) [52,53]. BEM is a fast and more accurate method compared to the Finite Element Method (FEM) or Finite Difference Method (FDM). This is due to the fact that BEM only needs to solve for the surface charges on the electrode surfaces. With FEM/FDM the Laplace equation has to be solved on a three dimensional mesh. Comparison of the speed and accuracy can be found in [54]. In order to simplify the variation and optimization of the trap geometry we have implemented a free scriptable object oriented BEM package for 3D and 2D [55]. We have verified the results for the geometry of Fig. 3 of our package against the results of the commercial BEM program CPO [56] (see Fig. 14 c) and against the results of the commercial FEM program FEMLAB [57] (see Fig. 14 a). The higher values in the latter case are due to the inaccuracy of the finite element method itself.

References

[1] The roadmaps of US and EU are found at http://qist.lanl.gov/ and http://qist.ect.it/.

[2] F. Schmidt-Kaler, H. Häffner, M. Riebe, S. Gulde, G. P. T. Lancaster, T. Deuschle, C. Becher, C. F. Roos, J. Eschner, and R. Blatt, Nature **422**, 408 (2003).

[3] D. Leibfried, B. DeMarco, V. Meyer, D. Lucas, M. Barrett, J. Britton, W. M. Itano, B. Jelenkovic, C. Langer, T. Rosenband, and D. J. Wineland, Nature **422**, 412 (2003).

[4] C. F. Roos, M. Riebe, H. Häffner, W. Hänsel, J. Benhelm, G. P. T. Lancaster, C. Becher, F. Schmidt-Kaler, and R. Blatt, Science **304**, 1478 (2004).

[5] H. Häffner, F. Schmidt-Kaler, W. Hänsel, C.F. Roos, T. Körber, M. Chwalla, M. Riebe, J. Benhelm, U. D. Rapol, C. Becher, and R. Blatt, Appl. Phys. B **81**, 151 (2005).

[6] C. Langer, R. Ozeri, J. D. Jost, J. Chiaverini, B. DeMarco, A. Ben-Kish, R. B. Blakestad, J. Britton, D. B. Hume, W. M. Itano, D. Leibfried, R. Reichle, T. Rosenband, T. Schaetz, P. O. Schmidt, and D. J. Wineland, Phys. Rev. Lett. **95**, 060502 (2005).

[7] M. Riebe, H. Häffner, C. F. Roos, W. Hänsel, J. Benhelm, G. P. T. Lancaster, T. W. Körber, C. Becher, F. Schmidt-Kaler, D. F. V. James, and R. Blatt, Nature **429**, 734 (2004).

[8] M. D. Barrett, J. Chiaverini, T. Schaetz, J. Britton, W. M. Itano, J. D. Jost, E. Knill, C. Langer, D. Leibfried, R. Ozeri, and D. J. Wineland, Nature **429**, 737 (2004).

[9] C. A. Sackett, D. Kielpinski, B. E. King, C. Langer, V. Meyer, C. J. Myatt, M. Rowe, Q. A. Turchette, W. M. Itano, D. J. Wineland, and C. Monroe, Nature **404**, 256 (2000).

[10] P. C. Haljan, K.-A. Brickman, L. Deslauriers, P. J. Lee, and C. Monroe, Phys. Rev. Lett. **94**, 153602 (2005).

[11] D. Leibfried, M. D. Barrett, T. Schätz, J. Britton, J. Chiaverini, W. M. Itano, J. D. Jost, C. Langer, and D. J. Wineland, Science **304**, 1476 (2004).

[12] D. Leibfried, E. Knill, S. Seidelin, J. Britton, R. B. Blakestad, J. Chiaverini, D. B. Hume, W. M. Itano, J. D. Jost, C. Langer, R. Ozeri, R. Reichle, and D. J. Wineland, Nature **438**, 639 (2005).

[13] H. Häffner, W. Hänsel, C. F. Roos, J. Benhelm, D. Chek-al-kar, M. Chwalla, T. Körber, U. D. Rapol, M. Riebe, P. O. Schmidt, C. Becher, O. Gühne, W. Dür, and R. Blatt, Nature **438**, 643 (2005).

[14] D. Kielpinski, C. R. Monroe, and D. J. Wineland, Nature **417**, 709 (2002).

[15] I. Chuang, private communication.

[16] M. A. Rowe, A. Ben-Kish, B. DeMarco, D. Leibfried, V. Meyer, J. Beall, J. Britton, J. Hughes, W. M. Itano, B. Jelenkovic, C. Langer, T. Rosenband, and D. J. Wineland, Quantum Inf. Comput. **2**, 257 (2002).

[17] M. Barrett, B. L. DeMarco, T. Schätz, V. Meyer, D. Leibfried, J. Britton, J. Chiaverini, W. M. Itano, B. M. Jelenkovic, J. D. Jost, C. Langer, T. Rosenband, and D. J. Wineland, Phys. Rev. A **68**, 042302 (2003).

[18] M. Drewsen, A. Mortensen, R. Martinussen, P. Staanum, and J. L. Soerensen, Phys. Rev. Lett. **93**, 243201 (2004).

[19] D. Leibfried and T. Schätz, Phys. J. **3**, 23 (2004).

[20] D. Stick, W. K. Hensinger, S. Olmschenk, M. J. Madsen, K. Schwab, and C. Monroe, Nature Physics **2**, 36 (2006).

[21] J. Chiaverini, R. B. Blakestad, J. Britton, J. D. Jost, C. Langer, D. Leibfried, R. Ozeri, and D. J. Wineland, arXiv:quant-ph/0501147 and Quant. Inf. Comput. **5**(6), 419 (2005).

[22] M. J. Madsen, W. K. Hensinger, D. Stick, J. A. Rabchuk, and C. Monroe, Appl. Phys. B **78**, 639 (2004).

[23] C. E. Pearson, D. R. Leibrandt, W. S. Bakr, W. J. Mallard, K. R. Brown, and I. L. Chuang, Phys. Rev. A **73**, 032307 (2006), arXiv:quant-ph/0511018.

[24] S. Seidelin, J. Chiaverini, R. Reichle, J. J. Bollinger, D. Leibfried, J. Britton, J. H. Wesenberg, R. B. Blakestad, R. J. Epstein, D. B. Hume, J. D. Jost, C. Langer, R. Ozeri, N. Shiga, D. J. Wineland, arXiv:quant-ph/0601173.

[25] H. Mabuchi, N. Khaneja, Int. J. Robust Nonlinear Control **15**, 647 (2005).

[26] I. Cirac and P. Zoller, Phys. Rev. Lett. **74**, 4091 (1995).

[27] D. J. Wineland, C. Monroe, W. M. Itano, D. Leibfried, B. E. King, and D. M. Meekhof, J. Res. Nat. Inst. Stand. Tech. **103**, 259 (1998).

[28] W. K. Hensinger, S. Olmschenk, D. Stick, D. Hucul, M. Yeo, M. Acton, L. Deslauriers, C. Monroe, and J. Rabchuk, App. Phys. Lett. **88**, 034101 (2006).

[29] B. N. Chichkov, C. Momma, S. Nolte, F. von Alvensleben, and A. Tünnermann, Appl. Phys. A **63**, 109 (1996).

[30] A. Mortensen, F. Nielsen, T. Matthey, and M. Drewsen, Phys. Rev. Lett. **96**, 103001 (2006).

[31] R. Alheit, Th. Gudjons, S. Kleineidam, and G. Werth, Rapid Rapid Commun. Mass Spectrom. **10**, 583 (1996).

[32] J. Eschner, G. Morigi, F. Schmidt-Kaler, and R. Blatt, J. Opt. Soc. Am. B **20**, 1003 (2003).
[33] U. Poschinger et al., in preparation.
[34] J. P. Home and A. M. Steane, arXiv:quant-ph/0411102.
[35] W. Paul, Q. Osberghaus, and E. Fischer, Forschungsberichte des Wirtschafts- und Verkehrsministeriums Nordrhein-Westfalen, Vol. 415 (1958).
[36] D. Leibfried, R. Blatt, C. Monroe, and D. Wineland, Rev. Mod. Phys. **75**, 281 (2003).
[37] M. Drewsen, C. Brodersen, L. Hornekaer, J. S. Hangst, and J. P. Schiffer, Phys. Rev. Lett. **81**, 2878 (1998) and private communication: For this trap the drive U_{rf} is applied also to the DC electrodes with opposite phase (see Fig. 1).
[38] F. Schmidt-Kaler, H. Häffner, S. Gulde, M. Riebe, G. P. T. Lancaster, T. Deuschle, C. Becher, W. Hänsel, J. Eschner, C. F. Roos, and R. Blatt, Appl. Phys. **77**, 789 (2003).
[39] W. K. Hensinger, S. Olmschenk, D. Stick, D. Hucul, M. Yeo, M. Acton, L. Deslauriers, J. Rabchuk, and C. Monroe, Appl. Phys. Lett. **88**, 034101 (2006).
[40] D. Stick, W. K. Hensinger, S. Olmschenk, M. J. Madsen, K. Schwab, and C. Monroe, Nature Physics **2**, 36 (2006).
[41] T. Calarco, U. Dorner, P. S. Julienne, C. J. Williams, P. Zoller, Phys. Rev. A **70**, 012306 (2004).
[42] U. Dorner, T. Calarco, P. Zoller, A. Browaeys, and P. Grangier, J. Opt. B **7**, 341 (2005).
[43] D. Kirk, Optimal Control Theory – An Introduction (Dover Publications, Mineda, New York, 2004).
[44] D. J. Tannor, Introduction to Quantum Mechanics: A Time-dependent Perspective (University Science Books, Sausalito, 2006).
[45] S. E. Sklarz and D. J. Tannor, Phys. Rev. A **66**, 053619 (2002).
[46] R. Kosloff, J. Phys. Chem. **92**, 2087 (1988).
[47] B. M. Garraway, J. Phys. B **33**, 4447 (2000)
[48] T. E. Skinner, T. O. Reiss, B. Luy, N. Khaneja, and S. J. Glaser, J. Magn. Reson. **172**, 17 (2005).
[49] J. J. García-Ripoll, P. Zoller, and J. I. Cirac, Phys. Rev. Lett. **91**, 157901 (2003).
[50] C. Rangan, A. M. Bloch, C. Monroe, and P. H. Bucksbaum, Phys. Rev. Lett. **92**, 113004 (2004).
[51] Ch. Roos, Th. Zeiger, H. Rohde, H. C. Nägerl, J. Eschner, D. Leibfried, F. Schmidt-Kaler, and R. Blatt, Phys. Rev. Lett. **83**, 4713 (1999).
[52] C. Pozrikidis, A Practical Guide to Boundary Element Methods (Chapman & Hall/CRC, Boca Raton, London, New York, Washington D.C., 2002).
[53] B. Brkić, S. Taylor, J. F. Ralph, and N. France, Phys. Rev. A **73**, 012326 (2006).
[54] D. Cubric, B. Lencova, F. H. Read, and J. Zlamal, Nucl. Instr. Meth. Phys. Res. A **427**, 357 (1999).
[55] URL: http://www.uni-ulm.de/qiv/staff/ksinger/bem.
[56] CPO program, available at www.electronoptics.com.
[57] FEMLAB program, available at www.femlab.com.

